

Ly α forest bounds on sterile neutrino production via neutrino self-interactions

Priyank Parashari ^{1,*} Vera Gluscevic,^{1,2,3,†} Yue Zhang,⁴ Simeon Bird,⁵ Mikhail M. Ivanov,^{6,7} and Adam He¹

¹*Department of Physics & Astronomy, University of Southern California, Los Angeles, CA, 90089, USA*

²*Institute for Advanced Study, 1 Einstein Drive, Princeton, NJ 08540, USA*

³*Center for Computational Astrophysics, Flatiron Institute, 162 5th Avenue, New York, NY, 10010, USA*

⁴*Department of Physics, Carleton University, Ottawa, ON K1S 5B6, Canada*

⁵*Department of Physics and Astronomy, University of California Riverside, Riverside, CA 92521*

⁶*Center for Theoretical Physics – a Leinweber Institute,*

Massachusetts Institute of Technology, Cambridge, MA 02139, USA

⁷*The NSF AI Institute for Artificial Intelligence and Fundamental Interactions, Cambridge, MA 02139, USA*

Sterile neutrinos in the keV mass range have long been considered a well-motivated dark matter (DM) candidate. In this work, we explore a sterile neutrino production mechanism through active neutrino self-interactions in the early universe, assuming that they constitute the full DM abundance. We implement a self-consistent treatment of the sterile-neutrino free streaming and the active-neutrino self-interactions on structure formation, which yield a unique scale-dependent modification to the linear matter power spectrum. We then set bounds on this scenario using a combination of the cosmic microwave background and Ly α forest constraints. Specifically, we utilize the two recent likelihoods derived from eBOSS data: (i) an effective field theory (EFT) based full-shape likelihood and (ii) a compressed likelihood obtained from the PRIYA-simulation emulator. We produce some of the most stringent observational constraints to date on sterile neutrino DM, comparable to the bounds from the most stringent laboratory constraints.

Keywords: Cosmology, Dark matter, Sterile neutrino, Self-interaction, Lyman- α Forest

I. INTRODUCTION

The nature of dark matter (DM) remains one of the most profound open questions in modern cosmology and particle physics. Despite astrophysical and cosmological observations providing compelling evidence for the existence of DM, its fundamental properties remain unknown[1–4]. A sterile neutrino with mass in the keV range, having no direct interaction with the Standard Model particles but interacting feebly via mixing with active neutrinos, has been proposed as a well-motivated DM candidate [5–7]. Unlike the three thermally-produced active neutrinos of the Standard Model, the production of this hypothetical fourth neutrino state involves a non-thermal freeze-in mechanism via active-sterile neutrino oscillations. The sterile neutrino state ν_4 is characterized by its mass m_4 and a small mixing angle θ , and its mass eigenstate is defined as a linear combination of a predominantly sterile component ν_s and a tiny component of active neutrinos ν_a ,

$$|\nu_4\rangle = \cos\theta|\nu_s\rangle + \sin\theta|\nu_a\rangle. \quad (1)$$

Dodelson and Widrow [8] (DW) demonstrated that the sterile neutrino, whose properties make it a compelling DM candidate, can be produced with the full relic abundance of DM, provided the appropriate combination of mass and mixing angle. In the DW framework, the production through oscillations continues until the active

neutrinos decouple from the rest of the particles, leaving behind a relic abundance of sterile neutrino DM.

However, the original DW mechanism is now ruled out by observations. Most importantly, the same active-sterile oscillations responsible for sterile neutrino production would also lead to radiative decay of sterile neutrino into a neutrino and a photon, and an X-ray line-emission in overdense regions of the universe, such as galaxies and galaxy clusters [9]. Even a small mixing angle required to produce the observed DM abundance via DW mechanism in the early universe would generate a detectable X-ray signal at most particle masses; the full range of mixing angles required to produce the relic abundance of DM with masses $m_4 \gtrsim 2$ keV via the original DW mechanism is excluded by X-ray bounds [10–14]. Lower masses are also excluded by various small-scale-structure constraints, as discussed in more detail below [6, 15–27].

New mechanisms for sterile neutrino production beyond the original DW scenario have been proposed in the literature [28–39]. One of these mechanisms involves the introduction of self-interactions among active neutrinos, which can boost sterile production at a fixed mixing angle, and relax observational constraints by opening up new parameter space for this DM model [36–39]. Neutrino self-interactions are well-motivated in their own as they can naturally arise in extensions of the Standard Model, particularly in context of neutrino mass generation mechanisms, such as models involving Majoron-like states or additional scalar and gauge degrees of freedom [40, 41]. More recently, they have also been explored in cosmological studies, as they can affect the Hubble tension [42–47]. At the same time, neutrino self-interaction scenarios have also been extensively explored using both laboratory experiments [43, 45, 48–62] and cosmological

* ppriyank@usc.edu

† verag@ias.edu

observations [27, 42, 44, 46, 63–80].

In this work, we assume the scenario in which DM consists entirely of sterile neutrinos produced via oscillations with active neutrinos in the early universe. DM production is enhanced by the presence of neutrino self-interactions, which modify the in-medium properties and scattering rates of active neutrinos, thereby allowing efficient sterile neutrino DM production [36]. As in the original DW mechanism, the effective mixing angle, which controls DM production, is strongly suppressed at very early times, while particle interaction rates are high. Conversely, unlike in the original DW scenario, at very late times, once active neutrinos fall out of thermal equilibrium with the rest of the thermal plasma, the production can still continue, as long as the active neutrino self-interactions persist. This aspect of the model relaxes the relic DM abundance constraint on the mixing angle and allows for a range of mixing angles to achieve the correct DM abundance at a fixed particle mass, by the appropriate choice of the neutrino self-interaction strength. The final DM abundance for a given sterile neutrino mass thus depends on a combination of active-sterile mixing angle, the self-interaction mediator mass, and the coupling strength; see Fig. 1 for an illustration.

We explore the full range of effects this model has on structure formation. On the one hand, neutrino self-interactions produce scale-dependent modifications to the linear matter power spectrum $P(k)$, as discussed in the previous literature [42, 73, 78, 79]. On the other hand, sterile neutrinos suppress structure on small scales, akin to warm DM cosmologies, regardless of the details of their production mechanism, due to a significant free streaming length. The sterile neutrino DM mass, which primarily affects free streaming, is therefore constrained by small-scale structure observations, including the MW satellite galaxy abundance, phase space density derived for dwarf galaxies, Lyman- α (Ly α) forest observations, and strong lensing [6, 16–27].

To test all structure-related aspects of this scenario with observational data, we implement, for the first time, a self-consistent approach to simultaneously compute the effects of both sterile neutrinos and neutrino self-interactions on $P(k)$. Using this framework, we confront the full model with Ly α forest and cosmic microwave background (CMB) measurements. As a key novelty in this work, we employ constraints derived from two Ly α likelihoods: an effective field theory (EFT) based full-shape likelihood [81, 82] and a compressed likelihood derived from the PRIYA simulations [83, 84]. Both these likelihoods are based on measurements of the one-dimensional Ly α flux power spectrum from the Baryon Oscillation Spectroscopic Survey (BOSS) of the Sloan Digital Sky Survey (SDSS) DR14, including data from the extended BOSS (eBOSS) survey [85]. We derive the most stringent observational bounds on the active–sterile mixing angle in the context of the full model, surpassing the lower limits previously inferred from DM relic abundance and Big Bang nucleosynthesis (BBN) constraint on

mediator mass. Our constraints are also comparable to those obtained from a combination of laboratory based experimental limits on self-interactions and BBN constraint. When combined with independent constraints from X-ray observations [10–14] and MW satellite galaxy abundance [27], our constraints can rule out the majority of the parameter space for sterile-neutrino DM production. The key results are presented in Fig. 4.

This paper is organized as follows. In Section II, we introduce the model for sterile neutrino DM production in the presence of self-interacting neutrinos. In Section III, we describe the impact of this DM model on the matter power spectrum and outline the methodology used for its computation. Section IV presents the data sets used and analyses performed. We present our main results for the constraints on the sterile neutrino DM parameters and compare them with the existing bounds in Section V. Finally, Section VI summarizes our findings and discusses possible future directions.

II. MODEL

We focus on the sterile neutrino DM production mechanism proposed in Ref. [36]. This model introduces a new self-interaction among active neutrinos, described by the Lagrangian

$$\mathcal{L} \supset \frac{\lambda_\phi}{2} \nu_a \nu_a \phi, \quad (2)$$

where λ_ϕ denotes the strength of coupling to a new complex mediator ϕ with mass m_ϕ , and a corresponds to different lepton flavors: e, μ , and τ . A Fermi-like constant (or the effective coupling) is given by $G_{\text{eff}} = \lambda_\phi^2/m_\phi^2$, and the self-interaction rate through the new mediator is $\Gamma_{\phi\nu_a\nu_a} \propto G_{\text{eff}}^2$ for a heavy mediator; for a light mediator, there is a more complex dependence on λ_ϕ and m_ϕ , as described in Ref. [36]. This self-interaction allows for the efficient production of sterile neutrinos, so they can account for all of the DM in the present-day universe. In this scenario, DM can be produced via three distinct production channels, denoted in the original work as Case A (production through a heavy-mediator self-interaction), Case B (on-shell decay of a mediator with a suppressed in-medium mixing angle), and Case C (on-shell decay of a mediator with a mixing angle close to its vacuum value) [27, 36].

To track the abundance of DM, we use the modified Boltzmann equation at fixed energy [8, 27, 36, 86, 87],

$$\frac{df_{\nu_s}}{dz} = \frac{\Gamma_{\text{tot}}}{4Hz} \sin^2 2\theta_{\text{eff}} f_{\nu_a}, \quad (3)$$

where f_{ν_s} and f_{ν_a} are the phase-space distribution (PSD) functions for the sterile neutrino and active neutrinos, respectively. Here, H is the Hubble parameter; Γ_{tot} is the total interaction rate of active neutrinos, including both weak and self-interaction contributions; z is cosmological

redshift; T_γ and T_{ν_a} represent the photon temperature and active neutrino temperature, respectively, and they are equal at early times. Finally, θ_{eff} denotes the effective mixing angle within the hot plasma, given by

$$\sin^2 2\theta_{\text{eff}} \simeq \frac{\Delta^2 \sin^2 2\theta}{\Delta^2 \sin^2 2\theta + \Gamma^2/4 + (\Delta \cos 2\theta - V_T)^2}, \quad (4)$$

where θ represents its vacuum value; $\Delta = m_4^2/(2E)$ is the vacuum oscillation frequency; E is the neutrino energy; and V_T is the thermal potential of active neutrinos.

In this framework, DM production rate $\Gamma_{\text{prod.}} = \frac{1}{2}\Gamma_{\text{tot}} \sin^2 2\theta_{\text{eff}}$ is generally only significant within a finite temperature range—while both factors in this expression have a non-vanishing value—and it asymptotes to zero otherwise. Namely, at early times, the effective mixing angle given by Eq. (4) vanishes, as the interaction rates and the neutrino potential are both very high $\Gamma, V_T \gg \Delta$. Conversely, as the temperature drops at late times, $\Gamma, V_T \rightarrow 0$ and the effective mixing angle defaults to its vacuum value; at this time, the production stops since Γ_{tot} vanishes. Therefore, efficient production occurs only at a specific time when appropriate conditions are met.

To track DM production, we first integrate Eq. (3) over the redshift range where DM production is most efficient while DM is still ultra-relativistic, and obtain f_{ν_s} . The present relic abundance of the sterile neutrino DM is then calculated as

$$\Omega_c = \left(\frac{2891.2}{1.05 \times 10^{-5} h^2} \right) \frac{n_{\nu_s} m_4}{s} \text{GeV}^{-1} \quad (5)$$

where n_{ν_s} is the number density of sterile neutrinos, s is the entropy density of the universe, and h is the reduced Hubble parameter.

In this DM model, the abundance of DM relics depends on four parameters: m_4 , θ , λ_ϕ , and m_ϕ . Fig. 1 illustrates the characteristic \mathcal{S} -shaped curve that captures the relationship between λ_ϕ and m_ϕ , which is obtained by requiring that sterile neutrino DM is produced at a fixed DM abundance, $\Omega_c h^2 = 0.12$ [4]. We show this curve for a combination of three sterile neutrino masses and two mixing angles as labeled. Note that the values of m_4 , θ , and m_ϕ are chosen independently of each other, and the requirement to obtain the correct relic abundance is satisfied by computing the interactions strength λ_ϕ as a function of these three parameters. Different parts of the curves correspond to the three production channels discussed previously; for clarity, we draw the two diagonal gray lines to separate these regions: the region between the diagonal lines corresponds to Case B, the region below the lower diagonal line corresponds to case C, and the region above the upper line to Case A.

We note that, as expected, the increase in the mixing angle generally leads to a lower value of λ_ϕ (for a given mediator and sterile-neutrino mass) to maintain a fixed production rate and provide the required abundance of DM. Similarly, given the interaction rate scaling, higher

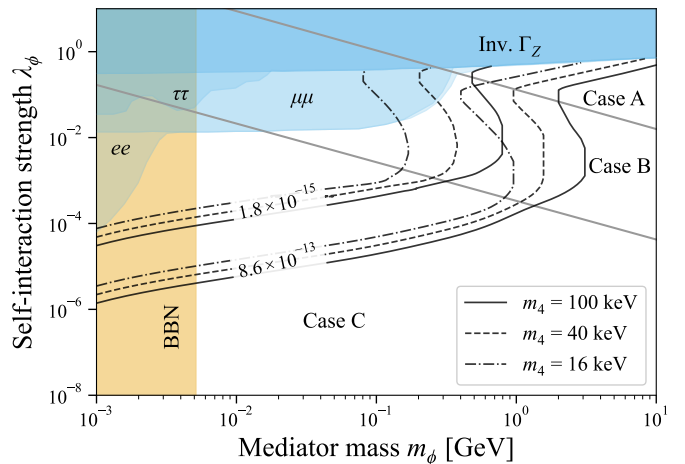


Figure 1. Self-interaction strength λ_ϕ required to produce the sterile neutrino DM consistent with observed DM relic density, $\Omega_c h^2 = 0.12$ [4], as a function of mediator mass, for several sterile-neutrino masses and mixing angles (listed in the legend). The characteristic \mathcal{S} -shaped curves shown by solid, dashed, and dot-dashed lines correspond to particle masses of $m_4 = 100, 40,$ and 16 keV, respectively; the curves are shown for two different values of $\sin^2(2\theta)$, as labeled in each set of curves. The gray solid lines separate the parameters space corresponding to the three production channels: Cases A, B, and C, as discussed in the text. The blue shaded regions are excluded by neutrino experiments involving the invisible Z decay ($\text{Inv. } \Gamma_Z$) and flavor-dependent constraints ($ee, \mu\mu,$ and $\tau\tau$ denote the type of flavor-specific coupling, corresponding to $\nu_e, \nu_\mu,$ and ν_τ , respectively) [43, 50, 58, 59]. The orange shaded region is inconsistent with BBN and the light-element-abundance measurements [36, 43, 66, 70].

values of λ_ϕ generally require higher values of m_ϕ .¹ We also show the portion of the parameter space excluded by various laboratory experiments as blue shaded region in the Figure [43, 45, 48–53, 55–60, 62]. The laboratory bounds include constraints from the decay width of invisible z-decay [43, 55, 62] and flavor-dependent constraints from observations of neutrino-less double β decay [51, 52], meson decays [43, 48, 53, 56, 57, 60] and τ -decay [43, 55]. The orange shaded region is excluded by the BBN and the measurements of the light element abundances [36, 43, 66, 70].

III. MATTER POWER SPECTRUM

The key observable on which we focus is the linear matter power spectrum $P(k)$. In this work, for the first time,

¹ A notable exception is Case B, where the interactions decouple while the mixing angle is still suppressed. In this case, the suppression of the mixing angle and the mediator mass pose competing effects that leads to the opposite proportionality between λ_ϕ and m_ϕ ; see Ref. [36] for details.

we compute the matter power spectrum simultaneously accounting for two effects: i) small-scale suppression of power resulting from sterile-neutrino DM free streaming and ii) scale-dependent enhancement and suppression of power at a *separate scale*, resulting from active neutrino self-interactions and their delayed decoupling. Both effects are illustrated in Fig. 2.

To compute the matter power spectrum $P(k)$ within this framework, we start with the implementation of the modified Boltzmann hierarchy equations for interacting active neutrinos from Ref. [42], into the publicly available CLASS code [78, 79, 88, 89]. We extend this code to include the model parameters $\Theta \in \{m_4, m_\phi, \lambda_\phi, \theta\}$ consistently. We note that the small-scale power cutoff is primarily controlled by the free streaming of sterile-neutrino DM, while the excess power primarily depends on the self-interaction strength; however, the two effects are not entirely independent of each other, as we can constrain Θ to always result in the given relic abundance of DM Ω_c . To ensure that this consistency relation is satisfied in our version of CLASS, we first determine the mixing angle required to produce a given Ω_c for any given set of $\{m_4, m_\phi, \lambda_\phi\}$. To achieve this within reasonable computational time, we build a neural network based emulator that predicts the correct mixing angle for the given values of $m_\phi, \lambda_\phi, m_4$, and Ω_c , trained on a large set of exact solutions obtained by directly solving Eq. (5). The emulator is then integrated as a part of our CLASS code, and is described in detail in an Appendix A. The next step involves the computation of (non-thermal) PSD of sterile neutrino for the resulting parameters and then feed it to the modified CLASS code to compute the matter power spectrum. We have consistently incorporated all these steps to build a robust pipeline for the computation of $P(k)$ within our sterile neutrino DM model.

In Fig. 2, we show the resulting $P(k)$ (normalized to the CDM case), for few reference sterile neutrino masses $m_4 = 10$ and 100 keV, and effective coupling $\log_{10}(G_{\text{eff}} \text{MeV}^2) = -2.0, -3.5$, and -5.0 . We see that as the value of G_{eff} increases, the excess power (the “bump”) feature that corresponds to the horizon scale at neutrino decoupling moves to smaller wavenumber k (decoupling at later times), whereas increasing the sterile neutrino mass shifts the cutoff to larger k (smaller length scales corresponding to a smaller free streaming length), as expected.

IV. DATA AND ANALYSIS

In this work, we leverage Ly α forest observations in combination with Planck CMB data [90] and CMB lensing data from the Atacama Cosmology Telescope (ACT) DR6 and Planck PR4 NPIPE [91–93] to assess the viable parameter space for this model. For Ly α , we employ two likelihoods derived using two different forward-modeling techniques, both based on the 1D Ly α flux power spectrum data from SDSS DR14 BOSS and

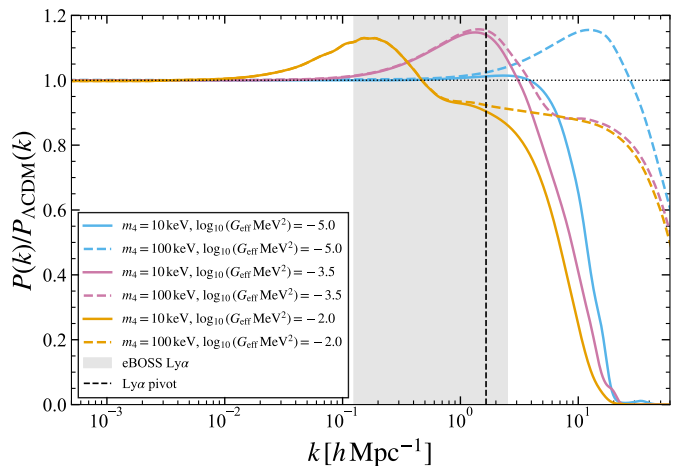


Figure 2. Ratio of the linear matter power spectrum in a cosmological model with sterile-neutrino DM and self-interacting neutrinos to the standard CDM case is shown for a range of DM particle masses m_4 and effective couplings G_{eff} , shown in the legend. The power spectra exhibit two key features: a bump, which depends on effective self-interaction coupling constant, and a sharp cutoff, related to the mass of sterile neutrinos. In each case, other model parameters are set such that neutrino DM has the observed DM relic abundance. The gray shaded region represents the scales probed by Ly α forest observations from the eBOSS survey [78, 79, 85]. The black dashed line denotes the pivot scale at which the reduced likelihood from the PRIYA simulation is evaluated [78, 79, 83, 84].

eBOSS [85] quasars. The first model is based on the EFT of large scale structure, and calibrated on Sherwood simulations [94, 95], with the associated likelihood based on eBOSS data from the redshift range $3.2 < z < 4.2$ [81, 82]; we label this likelihood as “Ly α -EFT” in our figures. The second model is based on the PRIYA simulation suite [83, 84], which provides a compressed likelihood in the form of Gaussian priors on the amplitude $\Delta_\star^2 = \frac{k_\star^3 P(k_\star, z_\star)}{2\pi^2}$ and slope $n_\star = \left. \frac{d \log P(k, z)}{d \log k} \right|_{k_\star, z_\star}^2$, evaluated at the pivot scale $k_\star = 0.009 \text{ s/km} \sim 1 \text{ Mpc}^{-1}$ and pivot redshift $z_\star = 3$ [79]; we label this case as “Ly α -PRIYA”.

As explained above, our model introduces four parameters ($m_4, m_\phi, \lambda_\phi, \theta$) in addition to the six standard cosmological parameters into the analysis. However, the requirement that sterile neutrinos are produced at the correct abundance Ω_c poses a constraint given by Eq. (5), which we use to fix the mixing angle. Furthermore, m_ϕ and λ_ϕ combine to set the effective coupling G_{eff} , leaving G_{eff}, m_4 and the six standard cosmological parameters as the only independent parameters of this cosmological model. We consider sterile neutrino mass range $m_4 \in [10, 1000] \text{ keV}$. In this mass range, modifications to

² These two quantities are denoted by Δ_L^2 and n_{eff} in Ref. [79].

the linear matter power spectrum due to sterile neutrino free streaming within the range of scales probed by the Ly α forest observations from the eBOSS survey are mild, and the onset of the full power suppression occurs at even smaller scales (higher k). This ensures that the PRIYA and EFT forward models can capture the full features of our model, and the modifications of $P(k)$ are well represented by the variation in amplitude and logarithmic tilt. Hence, we make use of the Markov Chain Monte Carlo (MCMC) chains generated by Ref. [79], which analyzed the self-interacting neutrino cosmology using the two Ly α likelihoods and CMB data. Since the previous analysis found no significant degeneracies between the parameters of the self-interacting neutrino model and Ω_c (or any other standard cosmological parameters), we chose not to resample the full cosmological posterior obtained in Ref. [79]. Instead, we translate the posteriors on G_{eff} and Ω_c into the constraints on the parameters of this model; we leave a more detailed exploration of the posterior for future work.

To translate the MCMC chain into constraints on the parameters of this model, we first randomly sample $m_\phi \in [10^{-3}, 10]$ GeV and $\lambda_\phi \in [10^{-9}, 1]$ retaining only those combinations that are consistent with the values of G_{eff} given in the original MCMC chains. For a given set of sterile neutrino mass $m_4 \in [10, 1000]$ keV, these selected values of m_ϕ and λ_ϕ , together with the corresponding value of Ω_c from the MCMC chains, are then passed to our emulator discussed in the previous section. The emulator returns the mixing angle required to reproduce the correct relic density. In this way, we construct derived MCMC chains for the parameters of our model. The resulting constraints are presented and discussed in detail in the next section.

V. RESULTS

Fig. 3 shows the 1-D and 2-D marginalized posteriors for $\omega_c = \Omega_c h^2$, $\log_{10}(G_{\text{eff}} \text{ MeV}^2)$, and $\log_{10}(\sin^2(2\theta))$ at 68% and 95% confidence level (C. L.), for Ly α -PRIYA (blue color) and Ly α -EFT (orange color) likelihoods, for sterile neutrino mass of $m_4 = 100$ keV. We repeat the analysis for a set of sterile neutrino mass values in the range 10–1000 keV, and obtain the lower limit on the mixing angle for each mass in Fig. 4. The two solid colored lines in that figure correspond to the two likelihoods considered in this work, and the shaded regions are excluded at 95% C. L.³

We note a few features of posterior probability distributions in Fig. 3. First, since $G_{\text{eff}} = \lambda_\phi^2/m_\phi^2$, the interaction strength and mediator mass are almost perfectly degenerate and cannot be constrained independently, so we

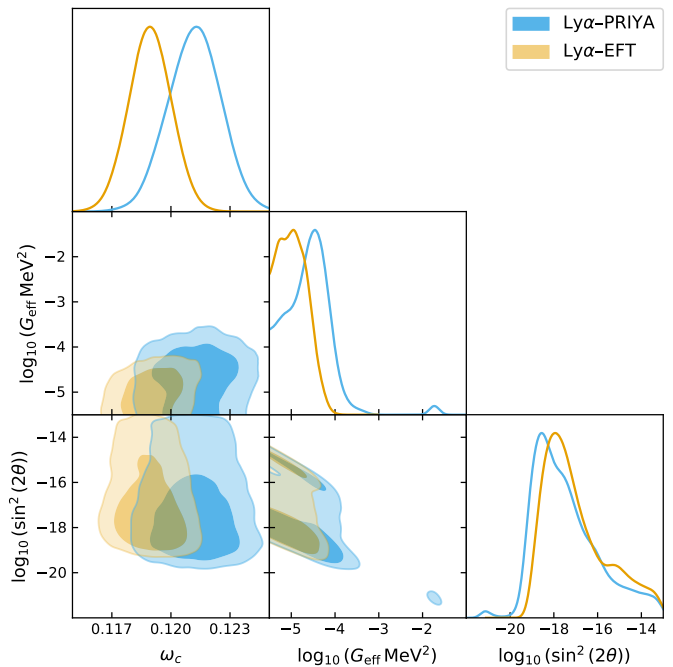


Figure 3. 1-D and 2-D marginalized posterior probability distributions for the active-sterile mixing angle, DM relic density, and the effective coupling constant between active neutrinos, assuming a sterile neutrino mass of $m_4 = 100$ keV. The two colors correspond to the results obtained using two different likelihoods based on eBOSS data: PRIYA-simulation and EFT-based likelihoods. The dark and light shaded regions denote the 68% and 95% C. L. contours, respectively.

omit them from the plots. We further see in Fig. 3 that ω_c values inferred from the two likelihoods are slightly different; this parameter is mainly constrained from CMB data, and the slight difference may be due to the slightly different σ_8 values preferred by the two Ly α likelihoods, and the degeneracy between ω_c and σ_8 ; see Ref. [79] for more details.

In addition, the posterior probability distribution for the mixing angle shows two modes, observed in Fig. 3. This feature flows directly from the non-trivial relationship between λ_ϕ and m_ϕ shown in Fig. 1: each mode corresponds to the dominance of a particular production channel for sterile neutrinos. In this model, the DM abundance no longer exhibits a one-to-one relationship between θ and Ω_c . Instead, for a given m_4 and G_{eff} consistent with observations, the correct DM can be produced through distinct channels corresponding to different values of θ . In particular, the lower- θ -value mode in the posterior is primarily associated with production through Cases B and C, while the higher θ value mode corresponds primarily to production through Case A. Since most of the higher θ values will be excluded by X-ray observations, Case A is largely ruled out, while the production through the C and B channels is still viable. This observation may provide further guidance for future model building in light of observational constraints.

³ Note that the small line thickness captures the emulator uncertainty in our predictions.

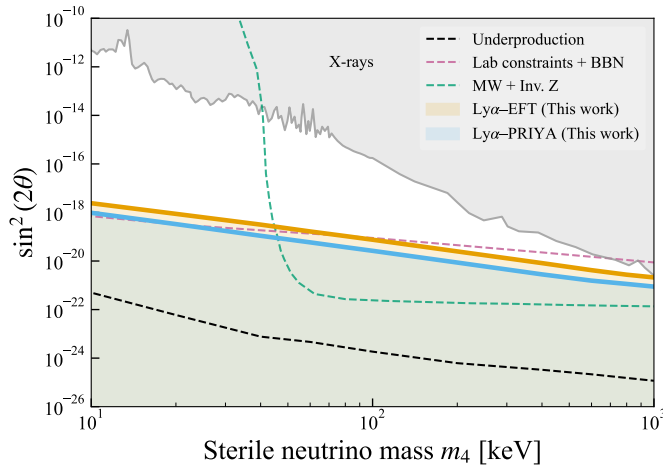


Figure 4. Constraints on sterile-neutrino DM from our analysis with $\text{Ly}\alpha$ forest observations. The two results of the current work are shown as the 95% C. L. lower bounds on the mixing angle between active and sterile neutrino, as a function of sterile-neutrino mass, obtained from the EFT and on PRIYA models and likelihoods, respectively. We also show the lower bound on the mixing angle from a combine analysis of BBN data [36, 43, 66, 70] with laboratory bounds on neutrino self-interactions [43, 50, 58, 59] (pink dashed line). The combined bound from MW satellite abundance and invisible Z decay from Ref. [27] is shown as the dashed green line; this bound is only valid under conditions discussed in the text. The black dashed line is lower bound on the mixing angle required to produce the observed DM abundance as measured by *Planck* [4]. The shaded gray region is ruled out by X-ray observations [10–14]. Overall, we note that the results of this work provide the most stringent observational bound in this parameter space, surpassing the underproduction limits from the CMB by several orders of magnitude. Note that the result is comparable to the most stringent laboratory constraints in the full sterile-neutrino mass range.

Finally, there is no upper bound on the mixing angle from this analysis—the upper limits seen in the triangle plots are an artifact resulting from the lack of posterior samples in that region of the parameter space, and the bound is *not* physical. However, the lower bound on the mixing angle is well sampled and robust.

Our main results are presented in Fig. 4. For comparison with our current constraints, this figure also shows the lower limit on the mixing angle derived from laboratory experiments [43, 50, 58, 59] and from primordial light element abundances [36, 43, 66, 70], shown in the pink dashed line and discussed in Section II. We further show the upper bound on mixing angles from X-ray observations [10–14] (gray shaded region), and the lower bound of the same parameter from DM abundance measurements⁴. The viable parameter space is represented by the white color in this Figure.

⁴ *Planck* measurement of DM relic abundance [4], combined with

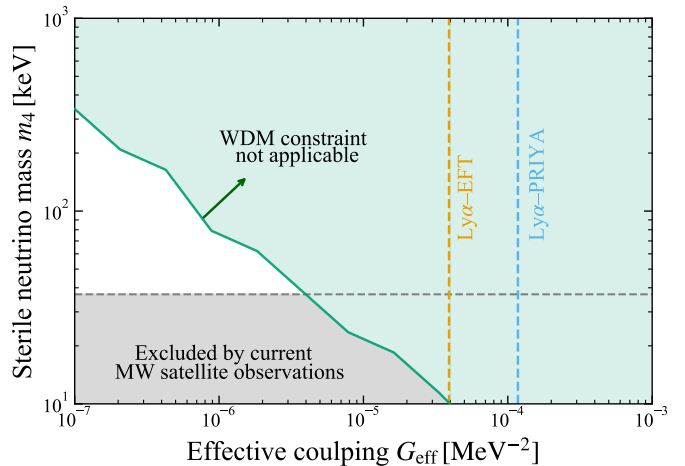


Figure 5. Schematic depiction of the m_4 – G_{eff} parameter space where constraints on sterile-neutrino DM obtained while neglecting self-interaction effects on the matter power spectrum (“bump feature”) are not applicable (green shaded region). The blue and orange dashed lines indicate the upper limit on the G_{eff} (at 95% C. L.) from the $\text{Ly}\alpha$ forest analysis, and the gray dashed line represent the lower bound on the sterile neutrino DM obtained from MW satellite abundances utilizing WDM simulations [27]. This bound can be applied to our model only where the effective coupling strength lies outside the green shaded region; within the shaded region, the power spectrum contains a feature that is not strictly modeled in the MW analysis. Gray shaded region represent the parameters space excluded by these MW bounds for our model.

Finally, we include in the same figure the combined constraint on sterile neutrinos from the MW satellite galaxy abundance and invisible z-decay as the green dashed line [27]. The MW satellite constraints were obtained using the warm DM (WDM) simulations. However, we note that the analysis in Ref. [27] did *not* model the effects of neutrino self-interactions on $P(k)$ and has only focused on the WDM-like cutoff at small scales. Therefore, this constraint strictly applies only to a portion of our parameter space where the bump feature induced by neutrino self-interaction is removed by the cutoff caused by DM free streaming. We show a schematic depiction of the applicability realm of the MW bound in our model in Fig. 5. For values of m_4 and G_{eff} within the green shaded region, labeled “WDM constraint not applicable”, in the same figure, a modeling of the MW satellite population in models with self-interactions is necessary to fully understand the bound on the sterile-neutrino mass. Hence, only the gray shaded part of m_4 – G_{eff} parameter space would be ruled out by the current MW constraint.

Overall, Fig. 4 demonstrates that the $\text{Ly}\alpha$ forest analyses presented in this work provide the most stringent ob-

light element abundance measurements [36, 43, 66, 70] implies an “underproduction” bound by imposing a lower limit for the mixing angle, for $\lambda_\phi \leq 1$ [36].

servational constraint on sterile-neutrino DM produced through active-neutrino self-interactions. This constraint surpasses the underproduction bounds from the DM relic density by several orders of magnitude, and is comparable to the bound obtained by combining the most stringent flavor-dependent laboratory constraints.

VI. CONCLUSIONS AND DISCUSSION

This work explored a specific model of sterile neutrino DM, where the production of the sterile neutrino is facilitated through a new self-interaction among active neutrinos [36]—a scenario well-motivated from the standpoint of neutrino mass production mechanisms. This model produces unique features in the matter power spectrum, testable by observational data. To understand the observational constraints on the model, we self-consistently include the effect of both the delay in active-neutrino free streaming due to a new self-interaction, and the effect of sterile-neutrino free streaming, in the computation of the linear matter power spectrum.

We then compare this model with Ly α forest observations. Specifically, we employ two Ly α likelihoods that measure the amplitude and shape of the linear matter power spectrum on small scales ($k \approx 0.1\text{--}2 \text{ hMpc}^{-1}$): an EFT-based full shaped likelihood [81, 82]; and a likelihood based on PRIYA simulation [83, 84]. Our analysis results in the strongest observational constraint on the sterile neutrino DM production to-date, comparable to the bounds obtained from flavor-dependent laboratory experiments [43, 50, 58, 59]; Fig. 4 shows our key result. When considered in conjunction with constraints from X-ray observations [10–14] and MW satellite abundance [27], a large portion of the viable parameter space for this model is ruled out.

Other observational bounds on the mass of sterile neutrino DM also exist, as discussed in Secs. I and V. We note that the strongest lower bounds on the sterile neutrino mass originate from measurements of small-scale structure, such as the MW satellite galaxy population [27], and the high-resolution Ly α forest measurements from BOSS and XQ-100 surveys [19, 21]. However, these previous studies model cosmologies with strict suppression of power at large k , where the power spectrum resembles that of warm DM; as a result, their bounds are *not* readily applicable to cosmologies with a more complex k -dependence, as the one we focus on in this work. The derivation of the mass bounds from these observables requires dedicated forward modeling of structure in cosmologies with both neutrino self-interaction and sterile neutrino free streaming and is enabled by the power spectrum calculation presented in this work. We leave a dedicated derivation of the new sterile-neutrino mass bound from high-resolution Ly α data to future work.

We further note a few potential caveats of our present analysis and outline directions for future work. Importantly, the compressed likelihood inferred from the

PRIYA simulation suite relies on simulations which varied the slope and amplitude of the matter power spectrum, without explicitly modeling self-interacting neutrinos. Ref. [79] tested the validity of approximating the effect of self-interacting neutrinos with a slope and amplitude shift. For their best-fit parameters with $\log_{10}(G_{\text{eff}} \text{ MeV}^2) \sim -5$, the approximation was good at $< 1\%$ over the redshift and scale ranges probed by the eBOSS Ly α forest [79]. The approximation is likely less accurate for the larger values of $\log_{10}(G_{\text{eff}} \text{ MeV}^2)$ shown in Fig. 2, but these values are strongly disfavored by the data. Our use of the PRIYA reduced likelihood is thus justified for our current purposes but should be re-assessed in future data analyses. By contrast, the EFT-based likelihood does not assume a particular shape for the matter power spectrum but uses a deterministic cosmology-independent relationship between the non-linear EFT parameters and the linear bias coefficient (motivated by the clustering of dark matter halos). These functions are calibrated on Sherwood and ACCEL2 cosmological simulations using a Planck-based cosmology [82, 96, 97]. In addition, the EFT-based likelihood also takes a different approach in modeling effects like patchy helium reionization and thus returns results that differ somewhat from PRIYA-based analyses [82, 96]. A detailed comparison between these two approaches is an ongoing research topic, and we leave detailed comparison of their results in the context of a specific cosmological model for future work.

Finally, we highlight that the Ly α forest cosmology is advancing at a rapid pace. Notably, DESI-based likelihoods are becoming available [98], with substantially improved systematic error control, as well as improved statistics. Furthermore, there are a range of observations available which probe even smaller length scales, constraining the existence of a cut-off in the matter power spectrum, as well as IGM thermodynamics [22, 26, 99–102, e.g.]. With several ongoing and forthcoming spectroscopic programs offering enhanced sensitivity and statistical power, Ly α forest cosmology promises increasingly stringent probes to the DM and beyond standard model physics scenarios.

ACKNOWLEDGMENTS

VG acknowledges the support from the National Science Foundation (NSF) CAREER Grant No. PHY-2239205, and from the Research Corporation for Science Advancement under the Cottrell Scholar Program. This publication was made possible through the support of Grant 63667 from the John Templeton Foundation. The opinions expressed in this publication are those of the author(s) and do not necessarily reflect the views of the John Templeton Foundation. YZ is supported by a Subatomic Physics Discovery Grant (individual) from the Natural Sciences and Engineering Research Council of Canada.

- [1] G. Bertone, D. Hooper and J. Silk, *Particle dark matter: Evidence, candidates and constraints*, *Phys. Rept.* **405** (2005) 279–390, [[hep-ph/0404175](#)].
- [2] G. Bertone and D. Hooper, *History of dark matter*, *Rev. Mod. Phys.* **90** (2018) 045002, [[1605.04909](#)].
- [3] M. Cirelli, A. Strumia and J. Zupan, *Dark Matter*, *arXiv preprint* (2024), [[2406.01705](#)].
- [4] PLANCK collaboration, N. Aghanim et al., *Planck 2018 results. VI. Cosmological parameters*, *Astron. Astrophys.* **641** (2020) A6, [[1807.06209](#)].
- [5] J. E. Gunn, B. W. Lee, I. Lerche, D. N. Schramm and G. Steigman, *Some Astrophysical Consequences of the Existence of a Heavy Stable Neutral Lepton*, *ApJ* **223** (1978) 1015–1031.
- [6] S. Tremaine and J. E. Gunn, *Dynamical Role of Light Neutral Leptons in Cosmology*, *Phys. Rev. Lett.* **42** (1979) 407–410.
- [7] K. N. Abazajian, *Sterile neutrinos in cosmology*, *Phys. Rept.* **711–712** (2017) 1–28, [[1705.01837](#)].
- [8] S. Dodelson and L. M. Widrow, *Sterile neutrinos as dark matter*, *Phys. Rev. Lett.* **72** (Jan., 1994) 17–20, [[hep-ph/9303287](#)].
- [9] P. B. Pal and L. Wolfenstein, *Radiative Decays of Massive Neutrinos*, *Phys. Rev. D* **25** (1982) 766.
- [10] A. Boyarsky, A. Neronov, O. Ruchayskiy and M. Shaposhnikov, *Constraints on sterile neutrino as a dark matter candidate from the diffuse x-ray background*, *MNRAS* **370** (2006) 213–218, [[astro-ph/0512509](#)].
- [11] C. R. Watson, Z. Li and N. K. Polley, *Constraining sterile neutrino warm dark matter with Chandra observations of the Andromeda galaxy*, *J. Cosmology Astropart. Phys.* **2012** (Mar., 2012) 018, [[1111.4217](#)].
- [12] S. Horiuchi, P. J. Humphrey, J. Onorbe, K. N. Abazajian, M. Kaplinghat and S. Garrison-Kimmel, *Sterile neutrino dark matter bounds from galaxies of the Local Group*, *Phys. Rev. D* **89** (2014) 025017, [[1311.0282](#)].
- [13] K. Perez, K. C. Y. Ng, J. F. Beacom, C. Hersh, S. Horiuchi and R. Krivonos, *Almost closing the ν MSM sterile neutrino dark matter window with NuSTAR*, *Phys. Rev. D* **95** (2017) 123002, [[1609.00667](#)].
- [14] C. Dessert, N. L. Rodd and B. R. Safdi, *The dark matter interpretation of the 3.5-keV line is inconsistent with blank-sky observations*, *Science* **367** (Mar., 2020) 1465–1467, [[1812.06976](#)].
- [15] E. O. Nadler, V. Gluscevic, K. K. Boddy and R. H. Wechsler, *Constraints on Dark Matter Microphysics from the Milky Way Satellite Population*, *ApJ* **878** (2019) 32, [[1904.10000](#)].
- [16] A. Boyarsky, O. Ruchayskiy and D. Iakubovskiy, *A Lower bound on the mass of Dark Matter particles*, *JCAP* **03** (2009) 005, [[0808.3902](#)].
- [17] C. R. Watson, Z.-Y. Li and N. K. Polley, *Constraining Sterile Neutrino Warm Dark Matter with Chandra Observations of the Andromeda Galaxy*, *JCAP* **03** (2012) 018, [[1111.4217](#)].
- [18] M. Viel, G. D. Becker, J. S. Bolton and M. G. Haehnelt, *Warm dark matter as a solution to the small scale crisis: New constraints from high redshift Lyman- α forest data*, *Phys. Rev. D* **88** (2013) 043502, [[1306.2314](#)].
- [19] J. Baur, N. Palanque-Delabrouille, C. Yèche, C. Magneville and M. Viel, *Lyman-alpha Forests cool Warm Dark Matter*, *JCAP* **08** (2016) 012, [[1512.01981](#)].
- [20] S. Horiuchi, B. Bozek, K. N. Abazajian, M. Boylan-Kolchin, J. S. Bullock, S. Garrison-Kimmel et al., *Properties of resonantly produced sterile neutrino dark matter subhaloes*, *Mon. Not. Roy. Astron. Soc.* **456** (2016) 4346–4353, [[1512.04548](#)].
- [21] C. Yèche, N. Palanque-Delabrouille, J. Baur and H. du Mas des Bourboux, *Constraints on neutrino masses from Lyman-alpha forest power spectrum with BOSS and XQ-100*, *JCAP* **06** (2017) 047, [[1702.03314](#)].
- [22] V. Iršič et al., *New Constraints on the free-streaming of warm dark matter from intermediate and small scale Lyman- α forest data*, *Phys. Rev. D* **96** (2017) 023522, [[1702.01764](#)].
- [23] DES collaboration, E. O. Nadler et al., *Milky Way Satellite Census. III. Constraints on Dark Matter Properties from Observations of Milky Way Satellite Galaxies*, *Phys. Rev. Lett.* **126** (2021) 091101, [[2008.00022](#)].
- [24] E. O. Nadler, S. Birrer, D. Gilman, R. H. Wechsler, X. Du, A. Benson et al., *Dark Matter Constraints from a Unified Analysis of Strong Gravitational Lenses and Milky Way Satellite Galaxies*, *ApJ* **917** (2021) 7, [[2101.07810](#)].
- [25] B. Villaseñor, B. Robertson, P. Madau and E. Schneider, *New constraints on warm dark matter from the Lyman- α forest power spectrum*, *Phys. Rev. D* **108** (2023) 023502, [[2209.14220](#)].
- [26] V. Iršič et al., *Unveiling dark matter free streaming at the smallest scales with the high redshift Lyman-alpha forest*, *Phys. Rev. D* **109** (2024) 043511, [[2309.04533](#)].
- [27] R. An, V. Gluscevic, E. O. Nadler and Y. Zhang, *Can Neutrino Self-interactions Save Sterile Neutrino Dark Matter?*, *Astrophys. J. Lett.* **954** (2023) L18, [[2301.08299](#)].
- [28] X.-D. Shi and G. M. Fuller, *A New dark matter candidate: Nonthermal sterile neutrinos*, *Phys. Rev. Lett.* **82** (1999) 2832–2835, [[astro-ph/9810076](#)].
- [29] M. Shaposhnikov and I. Tkachev, *The ν MSM, inflation, and dark matter*, *Phys. Rev. B* **639** (2006) 414–417, [[hep-ph/0604236](#)].
- [30] T. Asaka, M. Shaposhnikov and A. Kusenko, *Opening a new window for warm dark matter*, *Phys. Rev. B* **638** (2006) 401–406, [[hep-ph/0602150](#)].
- [31] F. Bezrukov, H. Hettmansperger and M. Lindner, *keV sterile neutrino Dark Matter in gauge extensions of the Standard Model*, *Phys. Rev. D* **81** (2010) 085032, [[0912.4415](#)].
- [32] M. Nemevsek, G. Senjanovic and Y. Zhang, *Warm Dark Matter in Low Scale Left-Right Theory*, *JCAP* **07** (2012) 006, [[1205.0844](#)].
- [33] S. B. Roland, B. Shakya and J. D. Wells, *Neutrino Masses and Sterile Neutrino Dark Matter from the PeV Scale*, *Phys. Rev. D* **92** (2015) 113009, [[1412.4791](#)].

- [34] J. A. Dror, D. Dunsky, L. J. Hall and K. Harigaya, *Sterile Neutrino Dark Matter in Left-Right Theories*, *JHEP* **07** (2020) 168, [2004.09511].
- [35] M. Nemevšek and Y. Zhang, *Dark Matter Dilution Mechanism through the Lens of Large-Scale Structure*, *Phys. Rev. Lett.* **130** (2023) 121002, [2206.11293].
- [36] A. de Gouvêa, M. Sen, W. Tangarife and Y. Zhang, *Dodelson-Widrow Mechanism in the Presence of Self-Interacting Neutrinos*, *Phys. Rev. Lett.* **124** (Feb., 2020) 081802, [1910.04901].
- [37] K. J. Kelly, M. Sen, W. Tangarife and Y. Zhang, *Origin of sterile neutrino dark matter via secret neutrino interactions with vector bosons*, *Phys. Rev. D* **101** (June, 2020) 115031, [2005.03681].
- [38] K. J. Kelly, M. Sen and Y. Zhang, *Intimate Relationship between Sterile Neutrino Dark Matter and ΔN_{eff}* , *Phys. Rev. Lett.* **127** (2021) 041101, [2011.02487].
- [39] C. Benso, W. Rodejohann, M. Sen and A. U. Ramachandran, *Sterile neutrino dark matter production in presence of nonstandard neutrino self-interactions: An EFT approach*, *Phys. Rev. D* **105** (2022) 055016, [2112.00758].
- [40] Y. Chikashige, R. N. Mohapatra and R. D. Peccei, *Are There Real Goldstone Bosons Associated with Broken Lepton Number?*, *Phys. Lett. B* **98** (1981) 265–268.
- [41] G. B. Gelmini and M. Roncadelli, *Left-Handed Neutrino Mass Scale and Spontaneously Broken Lepton Number*, *Phys. Lett. B* **99** (1981) 411–415.
- [42] C. D. Kreisch, F.-Y. Cyr-Racine and O. Doré, *Neutrino puzzle: Anomalies, interactions, and cosmological tensions*, *Phys. Rev. D* **101** (2020) 123505, [1902.00534].
- [43] N. Blinov, K. J. Kelly, G. Z. Krnjaic and S. D. McDermott, *Constraining the Self-Interacting Neutrino Interpretation of the Hubble Tension*, *Phys. Rev. Lett.* **123** (2019) 191102, [1905.02727].
- [44] A. Mazumdar, S. Mohanty and P. Parashari, *Flavour specific neutrino self-interaction: H_0 tension and IceCube*, *JCAP* **10** (2022) 011, [2011.13685].
- [45] K.-F. Lyu, E. Stamou and L.-T. Wang, *Self-interacting neutrinos: Solution to Hubble tension versus experimental constraints*, *Phys. Rev. D* **103** (2021) 015004, [2004.10868].
- [46] T. Brinckmann, J. H. Chang and M. LoVerde, *Self-interacting neutrinos, the Hubble parameter tension, and the cosmic microwave background*, *Phys. Rev. D* **104** (2021) 063523, [2012.11830].
- [47] A. Das and S. Ghosh, *Self-interacting neutrinos as a solution to the Hubble tension?*, *PoS EPS-HEP2021* (2022) 124, [2109.03263].
- [48] V. D. Barger, W.-Y. Keung and S. Pakvasa, *Majoron Emission by Neutrinos*, *Phys. Rev. D* **25** (1982) 907.
- [49] ALEPH, DELPHI, L3, OPAL, SLD, LEP ELECTROWEAK WORKING GROUP, SLD ELECTROWEAK GROUP, SLD HEAVY FLAVOUR GROUP collaboration, S. Schael et al., *Precision electroweak measurements on the Z resonance*, *Phys. Rept.* **427** (2006) 257–454, [hep-ex/0509008].
- [50] J. M. Berryman, A. de Gouvêa, K. J. Kelly and Y. Zhang, *Lepton-number-charged scalars and neutrino beamstrahlung*, *Phys. Rev. D* **97** (Apr., 2018) 075030, [1802.00009].
- [51] M. Agostini et al., *Results on $\beta\beta$ decay with emission of two neutrinos or Majorons in ^{76}Ge from GERDA Phase I*, *Eur. Phys. J. C* **75** (2015) 416, [1501.02345].
- [52] K. Blum, Y. Nir and M. Shavit, *Neutrinoless double-beta decay with massive scalar emission*, *Phys. Lett. B* **785** (2018) 354–361, [1802.08019].
- [53] J. M. Berryman, A. De Gouvêa, K. J. Kelly and Y. Zhang, *Lepton-Number-Charged Scalars and Neutrino Beamstrahlung*, *Phys. Rev. D* **97** (2018) 075030, [1802.00009].
- [54] B. Chauhan and S. Mohanty, *Signature of light sterile neutrinos at IceCube*, *Phys. Rev. D* **98** (2018) 083021, [1808.04774].
- [55] V. Brdar, M. Lindner, S. Vogl and X.-J. Xu, *Revisiting neutrino self-interaction constraints from Z and τ decays*, *Phys. Rev. D* **101** (2020) 115001, [2003.05339].
- [56] PIENU collaboration, A. Aguilar-Arevalo et al., *Search for the rare decays $\pi^+ \rightarrow \mu^+ \nu_\mu \nu \bar{\nu}$ and $\pi^+ \rightarrow e^+ \nu_e \nu \bar{\nu}$* , *Phys. Rev. D* **102** (2020) 012001, [2006.00389].
- [57] NA62 collaboration, E. Cortina Gil et al., *Search for K^+ decays to a muon and invisible particles*, *Phys. Lett. B* **816** (2021) 136259, [2101.12304].
- [58] I. Esteban, S. Pandey, V. Brdar and J. F. Beacom, *Probing secret interactions of astrophysical neutrinos in the high-statistics era*, *Phys. Rev. D* **104** (2021) 123014, [2107.13568].
- [59] J. M. Berryman et al., *Neutrino Self-Interactions: A White Paper*, in *2022 Snowmass Summer Study*, 3, 2022. 2203.01955.
- [60] P. S. B. Dev, D. Kim, D. Sathyan, K. Sinha and Y. Zhang, *New laboratory constraints on neutrinophilic mediators*, *Phys. Lett. B* **868** (2025) 139765, [2407.12738].
- [61] B. Chauhan and P. Parashari, *Probing the cosmic sterile-neutrino background with IceCube*, *Phys. Rev. D* **112** (2025) 043043, [2409.12145].
- [62] S. Foroughi-Abari, K. J. Kelly and Y. Zhang, *Radiative Correction from Secret Neutrino Interactions and Implications for Neutrino-Scattering Experiments*, 2510.15023.
- [63] F.-Y. Cyr-Racine and K. Sigurdson, *Limits on Neutrino-Neutrino Scattering in the Early Universe*, *Phys. Rev. D* **90** (2014) 123533, [1306.1536].
- [64] M. Archidiacono and S. Hannestad, *Updated constraints on non-standard neutrino interactions from Planck*, *JCAP* **07** (2014) 046, [1311.3873].
- [65] L. Lancaster, F.-Y. Cyr-Racine, L. Knox and Z. Pan, *A tale of two modes: Neutrino free-streaming in the early universe*, *JCAP* **07** (2017) 033, [1704.06657].
- [66] G.-y. Huang, T. Ohlsson and S. Zhou, *Observational Constraints on Secret Neutrino Interactions from Big Bang Nucleosynthesis*, *Phys. Rev. D* **97** (2018) 075009, [1712.04792].
- [67] I. M. Oldengott, T. Tram, C. Rampf and Y. Y. Y. Wong, *Interacting neutrinos in cosmology: exact description and constraints*, *JCAP* **11** (2017) 027, [1706.02123].
- [68] A. Mazumdar, S. Mohanty and P. Parashari, *Inflation models in the light of self-interacting sterile neutrinos*, *Phys. Rev. D* **101** (2020) 083521, [1911.08512].
- [69] M. Park, C. D. Kreisch, J. Dunkley, B. Hadzhiyska and F.-Y. Cyr-Racine, *Λ CDM or self-interacting neutrinos: How CMB data can tell the two models apart*, *Phys. Rev. D* **100** (2019) 063524, [1904.02625].

- [70] M. Escudero and S. J. Witte, *A CMB search for the neutrino mass mechanism and its relation to the Hubble tension*, *Eur. Phys. J. C* **80** (2020) 294, [1909.04044].
- [71] A. Das and S. Ghosh, *Flavor-specific interaction favors strong neutrino self-coupling in the early universe*, *JCAP* **07** (2021) 038, [2011.12315].
- [72] C. D. Kreisch et al., *Atacama Cosmology Telescope: The persistence of neutrino self-interaction in cosmological measurements*, *Phys. Rev. D* **109** (2024) 043501, [2207.03164].
- [73] D. Camarena, F.-Y. Cyr-Racine and J. Houghteling, *Confronting self-interacting neutrinos with the full shape of the galaxy power spectrum*, *Phys. Rev. D* **108** (2023) 103535, [2309.03941].
- [74] A. Das and S. Ghosh, *The magnificent ACT of flavor-specific neutrino self-interaction*, *JCAP* **09** (2023) 042, [2303.08843].
- [75] D. Camarena and F.-Y. Cyr-Racine, *Strong constraints on a simple self-interacting neutrino cosmology*, *Phys. Rev. D* **111** (2025) 023504, [2403.05496].
- [76] G. Montefalcone, S. Ghosh, K. K. Boddy, D. W. R. Ho and Y. Tsai, *Directly Probing Neutrino Interactions through CMB Phase Shift Measurements*, **2509.20363**.
- [77] S. Libanore, S. Ghosh, E. D. Kovetz, K. K. Boddy and A. Raccanelli, *Joint 21-cm and CMB forecasts for constraining self-interacting massive neutrinos*, *Phys. Rev. D* **112** (2025) 063502, [2504.15348].
- [78] A. He, R. An, M. M. Ivanov and V. Gluscevic, *Self-interacting neutrinos in light of large-scale structure data*, *Phys. Rev. D* **109** (2024) 103527, [2309.03956].
- [79] A. He, M. M. Ivanov, S. Bird, R. An and V. Gluscevic, *Fresh look at neutrino self-interactions with the Lyman- α forest: Constraints from EFT and PRIYA simulations*, *Phys. Rev. D* **112** (2025) 063540, [2503.15592].
- [80] A. M. Whitford, C. Howlett, T. M. Davis, D. Camarena and F.-Y. Cyr-Racine, *Limits of self-interacting neutrinos from the BAO and CMB phase shift*, **2511.00800**.
- [81] M. M. Ivanov, *Lyman alpha forest power spectrum in effective field theory*, *Phys. Rev. D* **109** (2024) 023507, [2309.10133].
- [82] M. M. Ivanov, M. W. Toomey and N. G. Karaçaylı, *Fundamental Physics with the Lyman-Alpha Forest: Constraints on the Growth of Structure and Neutrino Masses from SDSS with Effective Field Theory*, *Phys. Rev. Lett.* **134** (2025) 091001, [2405.13208].
- [83] S. Bird, M. Fernandez, M.-F. Ho, M. Qezlou, R. Monadi, Y. Ni et al., *PRIYA: a new suite of Lyman- α forest simulations for cosmology*, *JCAP* **10** (2023) 037, [2306.05471].
- [84] M. A. Fernandez, S. Bird and M.-F. Ho, *Cosmological constraints from the eBOSS Lyman- α forest using the PRIYA simulations*, *JCAP* **07** (2024) 029, [2309.03943].
- [85] eBOSS collaboration, S. Chabanier et al., *The one-dimensional power spectrum from the SDSS DR14 Ly α forests*, *JCAP* **07** (2019) 017, [1812.03554].
- [86] K. Abazajian, *Production and evolution of perturbations of sterile neutrino dark matter*, *Phys. Rev. D* **73** (2006) 063506, [astro-ph/0511630].
- [87] R. S. L. Hansen and S. Vogl, *Thermalizing sterile neutrino dark matter*, *Phys. Rev. Lett.* **119** (2017) 251305, [1706.02707].
- [88] J. Lesgourgues, *The Cosmic Linear Anisotropy Solving System (CLASS) I: Overview*, *arXiv e-prints* (Apr., 2011) arXiv:1104.2932, [1104.2932].
- [89] D. Blas, J. Lesgourgues and T. Tram, *The Cosmic Linear Anisotropy Solving System (CLASS). Part II: Approximation schemes*, *J. Cosmology Astropart. Phys.* **2011** (July, 2011) 034, [1104.2933].
- [90] PLANCK collaboration, N. Aghanim et al., *Planck 2018 results. V. CMB power spectra and likelihoods*, *Astron. Astrophys.* **641** (2020) A5, [1907.12875].
- [91] ACT collaboration, M. S. Madhavacheril et al., *The Atacama Cosmology Telescope: DR6 Gravitational Lensing Map and Cosmological Parameters*, *Astrophys. J.* **962** (2024) 113, [2304.05203].
- [92] ACT collaboration, F. J. Qu et al., *The Atacama Cosmology Telescope: A Measurement of the DR6 CMB Lensing Power Spectrum and Its Implications for Structure Growth*, *Astrophys. J.* **962** (2024) 112, [2304.05202].
- [93] J. Carron, M. Mirmelstein and A. Lewis, *CMB lensing from Planck PR4 maps*, *JCAP* **09** (2022) 039, [2206.07773].
- [94] J. S. Bolton, E. Puchwein, D. Sijacki, M. G. Haehnelt, T.-S. Kim, A. Meiksin et al., *The Sherwood simulation suite: overview and data comparisons with the Lyman α forest at redshifts $2 \leq z \leq 5$* , *Mon. Not. Roy. Astron. Soc.* **464** (2017) 897–914, [1605.03462].
- [95] J. J. Givans, A. Font-Ribera, A. Slosar, L. Seeyave, C. Pedersen, K. K. Rogers et al., *Non-linearities in the Lyman- α forest and in its cross-correlation with dark matter halos*, *JCAP* **09** (2022) 070, [2205.00962].
- [96] R. de Belsunce, S.-F. Chen, M. M. Ivanov, C. Ravoux, S. Chabanier, J. Sexton et al., *Precision measurements of EFT parameters and BAO peak shifts for the Lyman- α forest*, *Phys. Rev. D* **111** (2025) 063524, [2412.06892].
- [97] R. de Belsunce, M. M. Ivanov, J. M. Sullivan, K. Akitsu and S.-F. Chen, *Modeling the Cosmological Lyman- α Forest at the Field Level*, **2507.00284**.
- [98] J. Chaves-Montero et al., *Cosmological analysis of the DESI DR1 Lyman alpha 1D power spectrum*, **2601.21432**.
- [99] K. K. Rogers and H. V. Peiris, *Strong Bound on Canonical Ultralight Axion Dark Matter from the Lyman-Alpha Forest*, *Phys. Rev. Lett.* **126** (2021) 071302, [2007.12705].
- [100] K. K. Rogers, C. Dvorkin and H. V. Peiris, *Limits on the Light Dark Matter–Proton Cross Section from Cosmic Large-Scale Structure*, *Phys. Rev. Lett.* **128** (2022) 171301, [2111.10386].
- [101] M.-F. Ho, M. Qezlou, S. Bird, Y. Yang, C. Avestruz, M. A. Fernandez et al., *Small-scale Lyman alpha forest cosmology with PRIYA: Constraints from XQ100 and KODIAQ-SQUAD one-dimensional flux power spectra*, **2509.18271**.
- [102] M. M. Ivanov and S. Trifinopoulos, *Effective Field Theory Constraints on Primordial Black Holes from the High-Redshift Lyman- α Forest*, **2508.04767**.
- [103] D. P. Kingma, *Adam: A method for stochastic optimization*, *arXiv preprint arXiv:1412.6980* (2014).
- [104] H. Robbins and S. Monro, *A stochastic approximation method*, *Annals of Mathematical Statistics* (1951)

400–407.

- [105] S. Ruder, *An overview of gradient descent optimization algorithms*, *arXiv preprint arXiv:1609.04747* (2016) .
- [106] A. Paszke, S. Gross, F. Massa, A. Lerer, J. Bradbury, G. Chanan et al., *Pytorch: An imperative style, high-performance deep learning library*, *Advances in neural information processing systems* **32** (2019) .
- [107] C. R. Harris, K. J. Millman, S. J. van der Walt, R. Gommers, P. Virtanen, D. Cournapeau et al., *Array programming with NumPy*, *Nature* **585** (Sept., 2020) 357–362.
- [108] Wes McKinney, *Data Structures for Statistical Computing in Python*, in *Proceedings of the 9th Python in Science Conference* (Stéfan van der Walt and Jarrod Millman, eds.), pp. 56 – 61, 2010. DOI.
- [109] T. pandas development team, *pandas-dev/pandas: Pandas*, .
- [110] F. Pedregosa, G. Varoquaux, A. Gramfort, V. Michel, B. Thirion, O. Grisel et al., *Scikit-learn: Machine learning in Python*, *Journal of Machine Learning Research* **12** (2011) 2825–2830.

Appendix A: Neural Network Emulator for Mixing Angle Prediction

This appendix describes the architecture, training, and testing of our neural network (NN)–based emulator designed to predict active–sterile mixing angles from four input parameters: m_4 , m_ϕ , λ_ϕ , and ω_c . We employ the emulator in place of the computationally expensive numerical procedure required to map a given DM relic density to a mixing angle.

To build this NN-based emulator, we first generate the data using the full mathematical model. We sample the input parameter space using the Latin Hypercube Sampling (LHS) technique in the ranges $m_\phi \in [10^{-3}, 10]\text{GeV}$, $m_4 \in [1, 1000]\text{keV}$, $\sin^2(2\theta) \in [10^{-25}, 10^{-6}]$ and $\omega_c \in [0.05, 0.16]$. For each sample point, we numerically solve Eq. (5) to find the coupling constant within the range $[10^{-9}, 1]$. LHS technique enables uniform and efficient sampling of this multidimensional input parameter space, avoiding clustering and undersampling in any region. To ensure comprehensive coverage of the parameter space, we apply logarithmic scaling to parameters spanning multiple orders of magnitude and linear sampling to those with narrower ranges. In total, we initially generate 30,000 combinations of input parameters. For a subset of these points, no root was found for λ_ϕ within the range considered. After discarding these points, the final dataset comprises 21,577 unique parameter combinations. Next, we structure our datasets with a four-dimensional input vector of $\{\log m_\phi, \log \lambda_\phi, \log m_4, \omega_c\}$ and a corresponding output value $\log \theta$. The dataset is randomly shuffled and divided into independent training, validation, and test sets, comprising 16,520, 2,360, and 2,697 samples, respectively. We normalize all three datasets using z-score standardization to facilitate efficient, optimal network training.

We employ a fully connected feed-forward NN. This network architecture comprises an input layer corresponding to the four input parameters ($\log m_\phi, \log \lambda_\phi, \log m_4, \omega_c$), multiple hidden layers with nonlinear activation functions, and a single output layer that produces a scalar output $\log \theta$. To capture the inherent nonlinearities in the parameter relationships, we employ the Rectified Linear Unit (ReLU) activation function in the hidden layers. The number of neurons per hidden layer is determined through hyperparameter optimization.

Next, we describe the training procedure and the optimization strategy. We use the Mean Squared Error (MSE) as a loss function for our regression model, defined as $\mathcal{L} = \frac{1}{N} \sum_{i=1}^N (\log_{10}(\theta_{\text{pred},i}) - \log_{10}(\theta_{\text{true},i}))^2$, where N denotes the number of samples. To minimize the loss function during the training process, we compare two optimization algorithms: Adam [103] and stochastic gradient descent (SGD) [104, 105]. Training is performed with mini-batches of batch size 32 and 64, which balance computational efficiency with accuracy in gradient estimation. To avoid overfitting, we also implement an early-

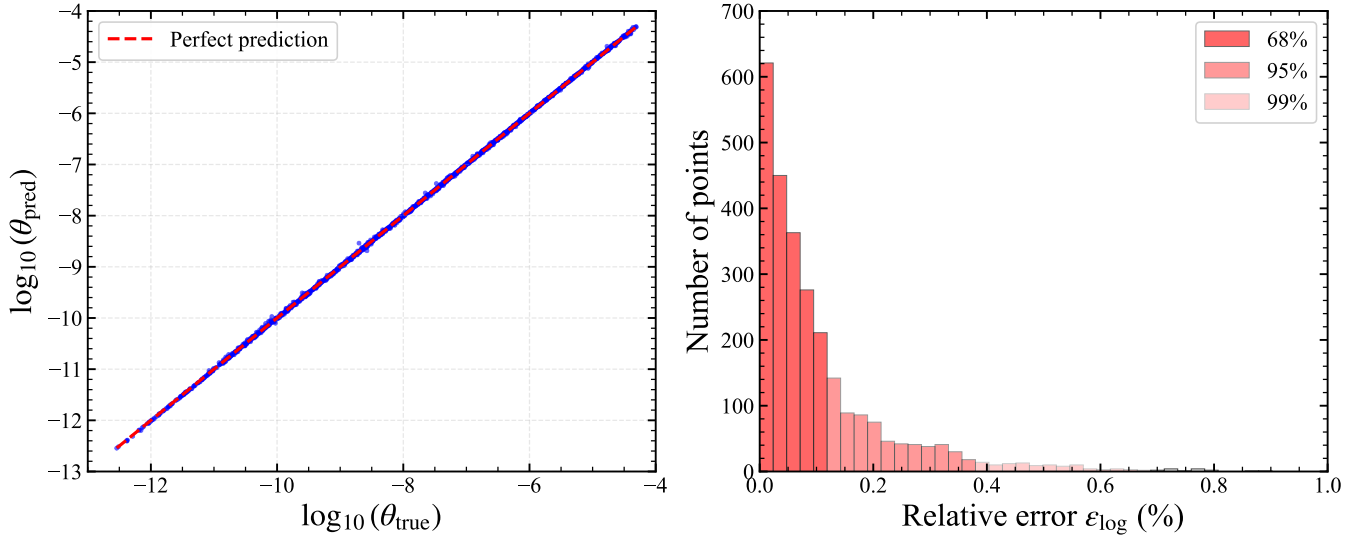


Figure 6. Prediction performance of the NN-based emulator for the active-sterile mixing angle on the independent test dataset. **Left panel:** Predicted values ($\log_{10}(\theta_{\text{pred}})$) plotted against the actual values $\log_{10}(\theta_{\text{true}})$ as shown by the blue points. The red dashed line represent the actual values from the test data. **Right panel:** Distribution of relative percentage errors ε_{\log} for the test data. The red shaded bands indicate regions with 68%, 95%, and 99% of the total number of test data (from darkest to lightest, respectively).

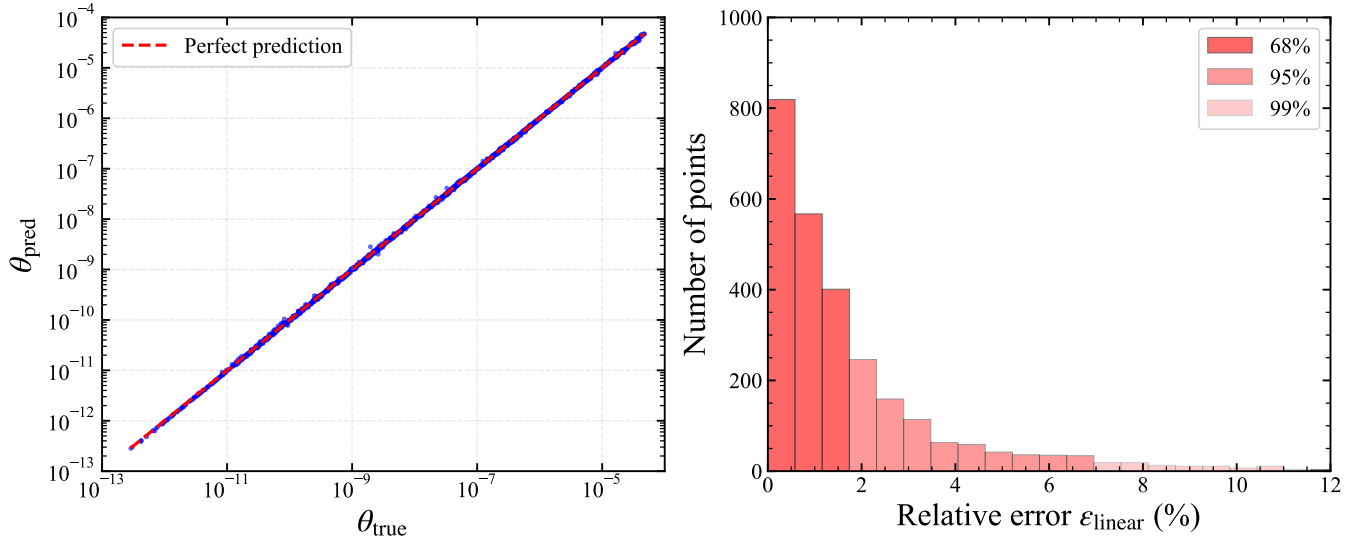


Figure 7. Prediction performance of the NN-based emulator for the active-sterile neutrino mixing angle on the independent test dataset. **Left panel:** Predicted values θ_{pred} plotted against the actual values θ_{true} as shown by the blue points. The red dashed line represent the actual θ values from the test data. **Right panel:** Distribution of relative percentage errors $\varepsilon_{\text{linear}}$ for the test data. The red shaded bands indicate regions with 68%, 95%, and 99% of the total number of test data (from darkest to lightest, respectively).

stopping mechanism with a maximum of 5000 epochs. The early stop mechanism uses a step-decay learning rate, which enables faster convergence and helps avoid overfitting. The initial learning rate is set to 0.01 and is reduced to 0.001 if no improvement in validation loss is observed for 150 consecutive epochs. A second reduction to 0.0001 occurs after another 150 epochs without

improvement in validation loss. Training terminates if no further improvement in validation loss is observed for 200 consecutive epochs. The final model is selected based on the weights corresponding to the minimum validation loss achieved during training.

We perform a systematic hyperparameter search using the training procedure described above to find the opti-

mal configuration of the NN model architecture. In this search, we fix the number of hidden layers at three and vary the number of neurons per hidden layer. We explore all combinations of 32, 64, and 128 neurons per layer, resulting in 27 distinct network configurations. For each configuration, we repeat the training process with both mini-batch sizes (32 and 64) and both optimization algorithms (Adam and SGD). The best-performing model is selected based on the lowest validation loss achieved across all configurations. The best NN architecture is found to be $4 \rightarrow 32 \rightarrow 128 \rightarrow 32 \rightarrow 1$, which corresponds to an input layer with four parameters, three hidden layers with 32, 128, and 32 neurons, respectively, and a single output.

The selected model is evaluated on the independent test data set. Fig. 6 (left panel) shows the predicted $\log_{10}(\theta_{\text{pred}})$ plotted against the corresponding actual values $\log_{10}(\theta_{\text{true}})$, while Fig. 7 (left panel) shows the same comparison in linear space (θ). The emulator achieves high prediction accuracy across the entire parameter

range. To quantify the prediction accuracy, we also compute the relative percentage error in both logarithmic and linear predictions as:

$$\varepsilon_{\log} = 100 \times \frac{|\log_{10}(\theta_{\text{true}}) - \log_{10}(\theta_{\text{pred}})|}{|\log_{10}(\theta_{\text{true}})|}, \quad (1)$$

$$\varepsilon_{\text{linear}} = 100 \times \frac{|\theta_{\text{true}} - \theta_{\text{pred}}|}{\theta_{\text{true}}}. \quad (2)$$

The distributions of the computed relative percentage errors are shown in the right panel of Fig. 6 and Fig. 7. The emulator predicts the mixing angle with less than 7% error for 95% times of the test samples, demonstrating excellent performance for the purposes of this work.

In conclusion, the NN-based emulator developed in this work provides an accurate and computationally efficient surrogate model to predict active sterile mixing angles. The emulator is implemented using Python with the following libraries: PyTorch [106], NumPy [107], pandas [108, 109], and Scikit-learn [110].